JACS
JOURNAL OF THE AMERICAN CHEMICAL SOCIETY

Article

pubs.acs.org/JACS

Correlations between Molecular Structure and Single-Junction Conductance: A Case Study with Oligo(phenylene-ethynylene)-Type Wires

Veerabhadrarao Kaliginedi,[†] Pavel Moreno-García,[†,‡,⊗] Hennie Valkenier,[§,⊥,⊗] Wenjing Hong,[†,⊗] Víctor M. García-Suárez,[∥,#,⊗] Petra Buiter,[§] Jelmer L. H. Otten,[§] Jan C. Hummelen,*[,§,⊥] Colin J. Lambert,*[,∥] and Thomas Wandlowski*[,†]

[†]Department of Chemistry and Biochemistry, University of Berne, Freiestrasse 3, CH-3012 Berne, Switzerland

[‡]Instituto de Física, Benemérita Universidad Autónoma de Puebla, Apartado Postal J-48, Puebla 72570, Mexico

[§]Stratingh Institute for Chemistry and [⊥]Zernike Institute for Advanced Materials, University of Groningen, Nijenborgh 4, 9747 AG Groningen, The Netherlands

[∥]Department of Physics, Lancaster University, Lancaster LA1 4YB, United Kingdom

[#]Departamento de Física, Universidad de Oviedo and CINN (CSIC), ES-33007 Oviedo, Spain

Supporting Information

ABSTRACT: The charge transport characteristics of 11 tailor-made dithiol-terminated oligo(phenylene-ethynylene) (OPE)-type molecules attached to two gold electrodes were studied at a solid/liquid interface in a combined approach using an STM break junction (STM-BJ) and a mechanically controlled break junction (MCBJ) setup. We designed and characterized 11 structurally distinct dithiol-terminated OPE-type molecules with varied length and HOMO/LUMO energy. Increase of the molecular length and/or of the HOMO−LUMO gap leads to a decrease of the single-junction conductance of the linearly conjugate acenes. The experimental data and simulations suggest a nonresonant tunneling mechanism involving hole transport through the molecular HOMO, with a decay constant $\beta = 3.4 \pm 0.1$ nm^{-1} and a contact resistance $R_c = 40$ kΩ per Au−S bond. The introduction of a cross-conjugated anthraquinone or a dihydroanthracene central unit results in lower conductance values, which are attributed to a destructive quantum interference phenomenon for the former and a broken π-conjugation for the latter. The statistical analysis of conductance−distance and current−voltage traces revealed details of evolution and breaking of molecular junctions. In particular, we explored the effect of stretching rate and junction stability. We compare our experimental results with DFT calculations using the ab initio code SMEAGOL and discuss how the structure of the molecular wires affects the conductance values.

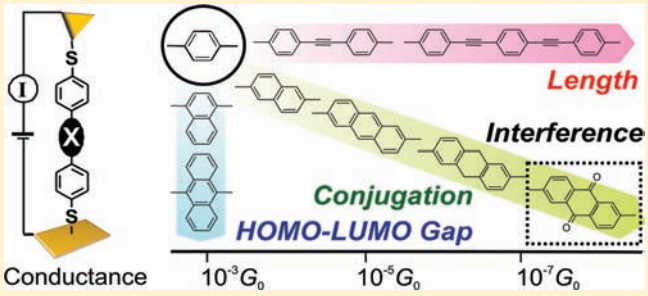

INTRODUCTION

Due to the intrinsic limitations of silicon-based electronics, the idea of using organic molecules as functional units in electronic devices has received increasing interest.[1] The detailed understanding of charge transport through single-molecule junctions is a key prerequisite for the design and development of molecular electronic devices. The implementation of (single) molecules and tailored molecular assemblies in electronic circuits requires the optimization of their structures toward desired functionalities and a reliable method of wiring them into nanoscale junctions.[2−10] In recent years, important correlations between transport properties and molecular structure have been demonstrated from the investigation of functional properties of single molecules and self-assembled monolayers.[11−13] Examples of reported functionalities illustrated by single molecules include diodes,[14−16] transistors,[17,18] memory effects,[19−21] and various switching phenomena, such as processes triggered by an electric potential,[22,23] the mechanical motion of a probe electrode,[24] or light excitation.[6,25,26] Furthermore, molecular wires are essential components for connecting functional units.[5] Oligo(phenylene-ethynylene) (OPE) compounds represent a particular unique family of molecular wires. They are fully π-conjugated rigid rod-like molecules with a HOMO−LUMO gap of ∼3 eV. Their structure and functional properties are tunable over a wide range of parameters.[27,28]

Various experimental approaches have been employed to investigate charge transport properties of OPE-type derivatives in molecular ensembles and at the single-molecule level.[10,11] The former include crossed wire configurations,[29] nanopores,[30] Au colloid arrays,[31] current−probe atomic force microscopy

Received: December 10, 2011
Published: February 21, 2012

   dx.doi.org/10.1021/ja211555x | J. Am. Chem. Soc. 2012, 134, 5262−5275

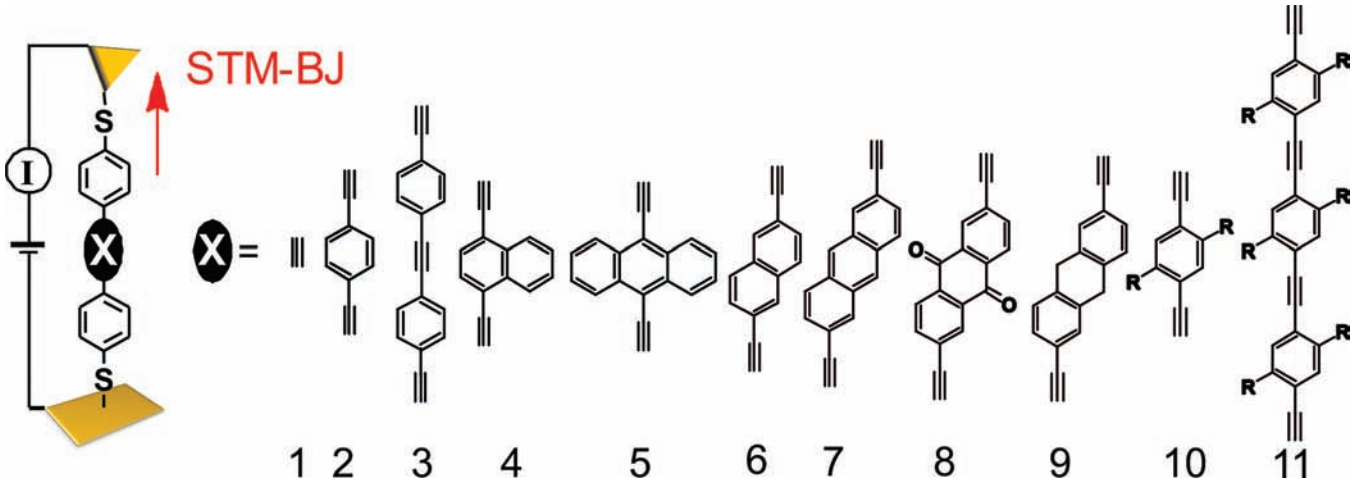

Figure 1. Structures of the OPE derivatives investigated. R = $CH_3(CH_2)_5O$.

(CP-AFM),[32−34] tuning fork-based techniques,[35] liquid metal junctions,[36] and molecular layers sandwiched between lithographically prepared contact electrode assemblies,[37] as well as a variety of electrochemical platforms.[38−40] Conductance experiments with single or a few OPE-type molecules have been addressed in matrix-isolation experiments,[41] mechanically controlled break junctions (MCBJ)[19,42−45] and STM break junctions (STM-BJ),[46−54] and related techniques. The experimental approaches mentioned above differ in the formation of reproducible contacts between the molecules and probe electrodes.[55] For the reliability of the data it is very important to demonstrate that the main features in "single"-junction conductance experiments do not suffer from "experimental artifacts". In particular, STM-BJ and MCBJ techniques provide access to measurements of a large number of individual conductance−distance and/or current−voltage traces under a wide range of conditions, enabling a robust and statistically relevant data analysis. Many configurations can be sampled and characterized quantitatively.

Due to different experimental techniques and data analysis procedures adopted by different groups, there are distinct differences in absolute values of conductances reported for single molecules and molecular assemblies. However, the search for trends in structure−conductance (and/or reactivity) correlations appears to be a very reliable and fruitful concept.[3,5,9,56] One of the key properties investigated is the length dependence of the molecular conductance. Systematic experimental and theoretical studies with thiol-terminated aliphatic and aromatic molecular wires suggested a nonresonant tunneling process as the main transport mechanism.[5,57] However, the tunneling decay parameter β in $G = A\ e^{-\beta L}$, with G and L as the molecular conductance and length, respectively, varied considerably. Examples of π-conjugated aromatic rods include a systematic study of $-NH_2$-terminated OPEs with β = 2.0 nm^{-1}.[51] Venkatamaran et al. reported a larger value of 4.0 nm^{-1} for oligophenylenes, in good agreement with calculations.[58] Alkoxy substituents at the central phenyl ring, which are often used to increase the solubility of OPE molecules, do not appear to influence the conductance values.[44] Smaller β values were found for oligoynes,[59] Zn-porphyrin-containing wires,[60] and oligothiophenes.[61] Related studies on a series of conjugated molecules have shown that the conductance decreases upon increasing the oxidation potential, i.e., upon lowering the energy of the HOMO level.[62] The influence of torsion angle φ was studied in several series of biphenyl derivatives. The authors found that the conductance follows a $\cos^2 \varphi$ correlation.[58,63,64] However, correlations between junction conductance, junction evolution, junction stability, and molecular structure were not clearly addressed. In particular, no comprehensive comparison of such results as obtained from two or more different experimental techniques (under the same experimental conditions) has been reported for rod-like molecules of the OPE family.

In the present work we investigate charge transport properties of 11 tailor-made dithiol-terminated OPE molecules (Figure 1) attached to two gold electrodes in complementary STM-BJ and MCBJ experiments. The family consists of structurally distinct molecules with varied lengths and energetics (HOMO−LUMO gap). The role of cross-conjugated building blocks is addressed as well. The statistical analysis of individual conductance−distance and current−voltage traces revealed details of the evolution and breaking of single molecular junctions. In particular, we explored the effect of stretching rate and junction stability. Finally, we compare our experimental results with DFT calculations using the ab initio code SMEAGOL, and discuss how the molecular junctions evolve upon stretching and how the structures of the molecular wires affect the junction transport characteristics.

EXPERIMENTAL SECTION

Chemicals and Synthesis. The molecular wires **1**−**7** were synthesized following the methodology developed by Stuhr-Hansen et al.[65,66] In short, the core of the molecular wire was constructed in a Sonogashira cross-coupling reaction, followed by conversion of the two *tert*-butyl-protected terminals (**1**−**9A**) into acetyl-protected dithiols (Scheme 1). The isolated yields of this step varied with the solubility of the compounds, ranging from 43% for **3** up to 91% for **1**. A slightly different protocol was used for **8** and **9**.[67] These air-stable compounds **1**−**9** can be deprotected to form dithiolates in situ.[37]

The synthesis of compounds **1** and **5** was reported by Stuhr-Hansen[66] and Mayor et al.[43] Detailed procedures and spectroscopic data of the molecules **1**, **3**, **4**, **6**, and **7** are given in the Supporting Information (SI). For the synthesis and characterization of **8** and **9** we refer to refs 56 and 68. The hexyloxy-substituted OPE rods **10** and **11** were obtained according to literature routes described by Zhou et al.[69]

All chemicals used in the synthesis were purchased from Aldrich, Acros, or Alfa-Aesar and employed as received, unless stated otherwise.

Conductance Measurements. The transport characteristics in single-molecule junctions were studied using STM-BJ and complementary MCBJ measurements, both in solution and at room

dx.doi.org/10.1021/ja211555x | J. Am. Chem. Soc. 2012, 134, 5262−5275

Scheme 1. Schematics of the General Synthesis of Molecular Wires 1−9[a]

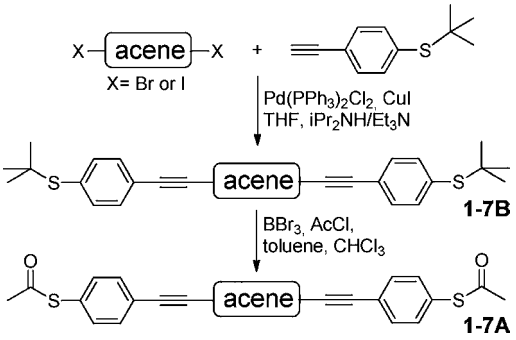

[a]**A** represents the acetyl-protected and **B** the *tert*-butyl-protected molecular wires.

temperature. The STM-BJ technique repeatedly traps molecules between a sharp STM tip and an atomically flat sample.[70,71] The MCBJ approach is based on the formation and breaking of molecular junctions between notched and freely suspended gold wires supported on insulated sheets of spring steel.[72,73]

The STM-BJ measurements were carried out with a Molecular Imaging PicoSPM housed in an all-glass argon-filled chamber and equipped with a dual preamplifier[74] capable of recording currents in a wide range of 1 pA to 150 μA with high resolution. The nonamplified low-current signal was fed back to the STM controller, preserving the STM imaging capability. The current−distance measurements were performed with a separate, lab-built analog ramp unit. For further technical details we refer to our previous work.[63,64]

The sample electrodes were Au(111) disks, 2 mm height and 10 mm in diameter, or gold single-crystal bead electrodes. The Au(111) substrates were flame-annealed prior to use. A freshly prepared solution containing typically a 0.1 mM concentration of the respective molecule (**1**−**11**) in a mixture of 1,3,5-trimethylbenzene (TMB, Aldrich, p.a.) and tetrahydrofuran (THF, Aldrich, p.a.), volume ratio 4:1, was added to a Kel-F flow-through liquid cell mounted on top of the sample. The STM tips were uncoated, electrochemically etched gold wires (Goodfellow, 99.999%, 0.25 mm diameter), capable of imaging with atomic resolution.

The following protocol was applied after assembling a new experiment: The tip was brought to a preset tunneling position typically defined by i_T = 50−100 pA and a bias voltage V_{bias} = 0.10 V, followed by imaging the substrate. Current−distance measurements were performed at a fixed lateral position with the STM feedback switched off and the vertical tip movement controlled by the ramp unit described above. The measuring cycle was performed in the following way: The controlling software drove the tip toward the adsorbate-modified surface. The approach was stopped when a predefined upper current limit was reached (typically 10 μA or <10G_0, with G_0 being the fundamental conductance quantum, 77.5 μS). After a short delay (∼100 ms) ensuring tip relaxation and the formation of stable contacts, the tip was retracted by 2−5 nm until a low current limit of ∼10 pA was reached. The approaching and withdrawing rates were varied from 2 to 160 nm/s. The entire current−distance traces were recorded with a digital oscilloscope (Yokogawa DL 750, 16 bit, 1 MHz sampling frequency) in blocks of 186 individual traces. Up to 2000 traces were recorded for each set of experimental conditions to guarantee the statistical significance of the results. For each molecule the data were acquired at three different bias voltages of 0.065, 0.100, and 0.170 V.

The MCBJ experiments are based on the opening and closing of nanogaps formed by notching a freely suspended, horizontally supported gold wire (99.999%, Goodfellow, 100 μm diameter) in a sample-molecule-containing solution, as controlled by the vertical movement of a pushing rod. The motion control is based on a combination of a stepper motor (Accu-coder 95511, Encoder Production, 500 nm s^{-1}) with a resolution of 5 nm per step and a moving distance of up to 1 cm, and a piezo stack on top (8 μm moving distance). The tunneling current between the two ends of the "broken wire", which act at a given bias voltage (typically between 0.020 and 0.200 V) as working electrodes WE1 and WE2, was utilized as a feedback signal. The pushing process started with the stepper motor. Once a current decrease was detected, which represents the breaking of the gold−gold contact, the stepper motor was paused, and the *z*-motion control was switched to the piezo stack. The voltage output of the piezo stack communicates with an onboard trigger. The latter senses the transport respective tunneling current and leads to the conductance. When the conductance reaches the noise threshold (G < $10^{-8}G_0$) or the high contact limit (set to $10G_0$), the voltage ramp for the piezo stack stops for a preset time of 0.5 s, and subsequently decreases or increases, respectively. The cycle is repeated more than 2000 times to obtain statistically relevant data.

The MCBJ controlling unit is based on a lab-built bipotentiostat with two bipolar tunable logarithmic I−V converters as current measuring units, which are operated by a custom-designed microcontroller.[74] The unit provides three analog signals. The first one controls the potential of WE1, which is particularly important for advanced electrochemical experiments with the MCBJ setup. The second one controls the voltage difference between the two working electrodes WE1 and WE2 (bias voltage V_{bias}), which drives the current through the two gold electrodes for the conductance measurements. The third channel controls the voltage output of the piezo stack in the range of 0−50 V, allowing the displacement of the piezo stack up to 8 μm with rates ranging from 3 to 3000 nm s^{-1}, which translates into lateral pulling (pushing) rates between the two gold leads of 0.1−100 nm s^{-1}, with a positional precision better than 0.05 nm. The distance between the two gold electrodes in the MCBJ setup was calibrated with complementary STM-BJ experiments assuming that the tunneling decay is identical under the same experimental conditions.

The entire setup was placed in two Faraday boxes, one for the mechanical unit and the other for the controller unit in order to avoid electronic cross-talk between the different functional parts. The full technical description of the setup is reported by Hong et al.[73]

The sample templates were spring steel sheets (30 mm × 10 mm × 0.2 mm), which were cleaned in boiling 25% nitric acid (Merck AG, 65%, pro analysis) and Milli-Q water (18.2 MΩ cm^{-1}, 2 ppb TOC), and dried in a stream of argon. A gold wire (Goodfellows 99.999%, 100 μm diameter) was fixed on these sheets with two drops of preheated epoxy (Stycast 2850FT with catalyst **9**) and cured overnight at 60 °C. The freely suspended part of the gold wire (less than 500 μm) was notched with a scalpel blade to fabricate a constriction point. The as-prepared sample sheets were cleaned in boiling Milli-Q water for 15 min, rinsed with isopropanol (Aldrich, pro analysis), dried with argon, and mounted on the sample holder of the MCBJ setup. Finally, the precleaned Kel-F liquid cell was installed on top of the sample with a Kalrez O-ring to avoid leakage of the solution. The closed liquid cell was flushed with argon through an inert cycling system to remove oxygen, and the test-molecule-containing solution was pumped into the cell in several cycles. Finally, the input and output valves for solution and gas purging were closed, and the experiment started.

Deprotection of the compounds **1**−**7** was carried out in situ by adding tetrabutylammonium hydroxide just before the start of the transport experiment in the STM configuration. For comparison, we also carried out complementary studies with molecules **1**−**11** employing both the STM-BJ and MCBJ setups in the absence of deprotecting agents.

Details of the data analysis are reported in the SI.

Theoretical Methods. The electronic and transport properties of the OPE derivatives were obtained using the ab initio code SMEAGOL,[75,76] which employs the Hamiltonian provided by the density functional theory (DFT) code SIESTA,[77] in combination with the nonequilibrium Green's function formalism. SIESTA uses nonconserving pseudopotentials to account for the core electrons, and a linear combination of pseudoatomic orbitals to span the valence states. The calculations used a single-ζ basis set for the gold leads, which included the s- and d-orbitals in the valence. An energy cutoff of

dx.doi.org/10.1021/ja211555x | J. Am. Chem. Soc. 2012, 134, 5262−5275

200 Ry was chosen to define the real-space grid, which is used to represent the density and the potential, and to calculate the Hamiltonian and the overlap matrix elements. The local density approximation (LDA)[78] was employed to account for exchange and correlation effects. The Fermi distribution function was smoothed with a temperature of 100 K to improve the convergence of the results. The molecular coordinates were relaxed in the isolated molecule until the forces were smaller than 0.05 eV/Å, and then included into the "extended molecule" without further relaxation. The system was made periodic along the perpendicular directions x and y, and only the gamma point was used. The "extended molecule" is represented by the dithiolated OPE compound bridged to five atomic gold layers to account for specific properties of the contact region such as adsorption geometry, molecular conformation, etc. Each layer contains 18 atoms, i.e., 6 and 3 atoms along each lattice vector on the (111) surface. This arrangement was necessary to avoid overlaps with molecular images along the perpendicular directions (see also SI).

SMEAGOL divides the entire nanoscale junction into three parts: the left and the right bulk electrodes, simulated by three gold layers grown along the (111) direction, and the "extended molecule". SMEAGOL uses the Hamiltonian derived from SIESTA to calculate self-consistently the density matrix, the transmission coefficients $T(E)$ of electrons from the left to the right lead, and the $I-V$ characteristics.

Corrected positions of the Fermi energy relative to the HOMO were obtained by applying a scissors-type operator to the bare DFT results (SAINT[79−81]) that moves the occupied and the unoccupied molecular levels downward and upward, respectively. The spectral adjustment was chosen to fit the position of such levels as obtained from a combination of experimental UV photoelectron spectroscopy (UPS), UV/vis absorption, and electrochemical data. Further details about the theoretical method and the energy level alignment are given in the SI.

RESULTS AND DISCUSSION

OPE Compound 2: Conductance Measurements and Molecular Junction Evolution. *Conductance Measurements Based on Stretching Traces.* Figure 2A displays typical conductance−distance stretching traces, plotted on a logarithmic scale, as recorded for the deprotected compound **2** in TMB/THF by the STM-BJ upon application of a bias voltage V_{bias} = 0.10 V between the gold STM tip and the Au(111) substrate. After the formation of the contact between the tip and the substrate, the tip was withdrawn with a rate v = 58 nm s^{-1}. All curves show initially a stepwise decrease of the conductance from ~$10G_0$ to $1G_0$, $G_0 = 2e^2/h$ = 77.5 μS being the quantum of conductance, with quantized conductance steps occurring at integer multiples of G_0. Structurally the evolution of the conductance corresponds to the decrease of the number of gold atoms in the constriction upon junction elongation until the contact with only one gold atom in the cross-section is formed. Subsequently, the current abruptly decreases by several orders of magnitude ("jump-out-of-contact") upon stretching, and additional features are typically observed at $G < 10^{-3}G_0$ before the conductance reaches the noise level of ~$10^{-7}G_0$.

We distinguish three types of measured curves: 25−30% of all traces exhibited after the "jump-out-of-contact" a bare tunneling current, exponentially decaying until the noise level is reached (type I, black traces in Figure 2A; type I curves are attributed to traces with no molecules trapped between the tip and substrate); 5−10% of all curves are rather noisy and exhibit fluctuations, which are typically attributed to mechanical instabilities (type II, gray); and the remaining 60−70% of all traces recorded show well-defined plateaus after breaking of the gold contact (type III, blue traces in Figure 2A). The plateaus occur in a narrow conductance range around $10^{-4}G_0$ and are characterized by a slight decrease of the conductance with

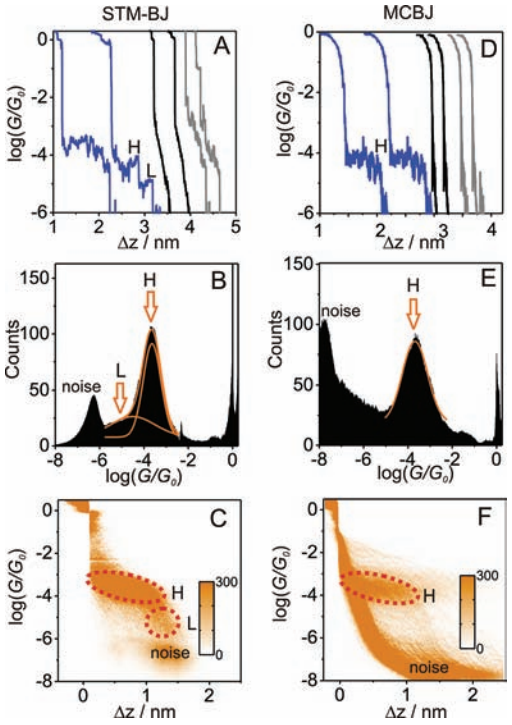

Figure 2. (A−C) Conductance measurements of **2** employing the STM-BJ approach. (A) Typical conductance distance traces recorded at V_{bias} = 0.1 V. (B) 1D conductance histogram and (C) 2D histogram generated from 2000 individual curves. (D−F) Conductance measurements of **2** employing the MCBJ approach. (D) Typical conductance distance traces measured at V_{bias} = 0.1 V. (E) 1D conductance histogram and (F) 2D conductance histograms generated from 2000 curves.

stretching distance Δz, before it drops abruptly. In 50% of these traces, short plateaus with conductances around $10^{-5}G_0$ were also observed. Both types of conductance plateau were absent in control experiments in the absence of compound **2**. We assign these plateaus to the conductance of junctions formed by molecules bridging the gap between the two gold electrodes.

Without any data selection, 2000 conductance−distance traces, measured under the same conditions, were analyzed further. Figure 2B displays the one-dimensional (1D) histogram of the logarithm of the conductance $\log(G/G_0)$[82] constructed from all data points of 2000 curves of **2** (V_{bias} = 0.10 V). The sharp peak in the histogram around 0 represents the conductance of a single-atom gold−gold contact.[83] The 1D histogram displays a prominent peak G_H with a maximum at 1.8 × $10^{-4}G_0$ (13.9 nS) and a shoulder at lower G in the entire range between 0 and −6 (in units of of $\log(G/G_0)$), the latter being the lower limit of a reliably measurably conductance in our STM-BJ setup (which is indicated as "noise" in Figure 2B,C). The shoulder was deconvoluted as a small peak centered at G_L = 9.7 × $10^{-6}G_0$ (0.76 nS) by fitting Gaussians to the histogram. We attribute G_H and G_L to the two most probable conductance states of a single molecule **2** bound to two gold leads. This assignment is supported by a two-dimensional (2D) histogram[64,84] constructed as follows. First, we normalized all individual conductance traces to a common distance scale by assigning $\Delta z = 0$ at $G = 0.7G_0$.[64] This procedure is justified by the sharp drop in conductance just after G_0. The conductance−distance histogram was then constructed by counting the

dx.doi.org/10.1021/ja211555x | J. Am. Chem. Soc. 2012, 134, 5262−5275

occurrence of $[\log(G/G_0);\Delta z]$ pairs in a 2D field. Further details of this analysis procedure are described in the SI.

2D histograms constructed from traces such as in Figure 2A (Figure 2C) show features of gold quantum contacts at $G \geq G_0$, a second main cloud-like feature at $[0 \leq \Delta z \leq 1.25$ nm; $10^{-3} G_0 \geq G \geq 2 \times 10^{-5} G_0]$ with a center around $1.2 \times 10^{-4} G_0$, and a satellite feature at $[1.10$ nm $\leq \Delta z \leq 1.25$ nm; $10^{-5} G_0 \geq G \geq 10^{-6} G_0]$ centered around $9.7 \times 10^{-6} G_0$. The latter two features correspond to the conductance peaks with maxima at G_H and G_L, as observed in the 1D histogram (Figure 2B). Note that the high-conductance feature H starts immediately after breaking of the gold–gold contact, while the low-conductance range L starts only after feature H at $\Delta z \approx 1.10$ nm. The experimentally observed decrease of the conductance in region H with increasing Δz (Figure 2C) might reflect a continuous decrease of the tilt angle between the "trapped" molecular wire **2** and the surface normal upon pulling.[52]

Complementary experiments were carried out with the acetyl-protected compound **2** in the STM-BJ and the MCBJ setups. The results of the MCBJ experiments are summarized in Figure 2D–F. The amount of curves displaying features of molecular junctions increases up to 80% of all measured curves, which we attribute to the overall higher mechanical stability of our MCBJ setup. We also note that the MCBJ setup has an electrical noise level of $\sim 10^{-8} G_0$ (indicated as "noise" in Figure 2E,F) and thus allows measurements of lower conductances than the STM-BJ setup. Individual traces (Figure 2D), the 1D histogram (Figure 2E), and the 2D histogram (Figure 2F) demonstrate a single peak with a maximum at $1.3 \times 10^{-4} G_0$ (10 nS) and a cloud-like feature at $[0 \leq \Delta z \leq 1.30$ nm; $10^{-3} G_0 \geq G \geq 3 \times 10^{-5} G_0]$ corresponding to the high conductance of molecular junctions, in good agreement with the STM-BJ experiments. No low-conductance feature was observed in experiments with the acetyl-protected molecular wire **2**. A similar observation was also reported by González et al.[54] However, the low-conductance junctions reappeared when the aromatic solvent TMB was replaced by the nonpolar aliphatic solvent decane (see SI).

Finally, we comment that the high-conductance value G_H for compound **2** reported here is comparable with values published previously by Tao and co-workers (6–13 nS),[46,85,86] Xing et al. (10 nS),[50] and Liu et al. (3.6 nS)[47] as based on STM-BJ measurements. Haiss et al.[52] found ~10 nS in their $I(t)$ and $I(s)$ experiments.[52,87] Huber et al.[44] and Wu et al.[45] obtained values of ~9 nS by an MCBJ technique.

The stability of molecular junctions formed by compound **2** attached to two gold electrodes was explored in the STM-BJ setup by varying the stretching rate v from 1 to 145 nm s^{-1}. The 1D histograms (Figure 3A) demonstrate that the most probable conductance values G_H and G_L are rather independent of the stretching rate (Figure 3B). However, the width (fwhm) of the corresponding histogram peaks increases slightly with decreasing v. This trend might reflect contributions of thermal fluctuations, atomic-scale variations in the geometry of the molecule–electrode contacts, conformation changes in the molecule, and other factors.[88]

A distinct rate dependence was obtained in STM-BJ experiments for the distance Δz over which the molecular junction could be stretched before breakdown (Figure 4).

The plot was constructed on the basis of a statistical analysis of all experimental conductance versus displacement traces (cf. 1D histogram in Figure 3 and the corresponding 2D histograms in SI, section 5) in $0.7G_0$ (the displacement Δz is set to zero at

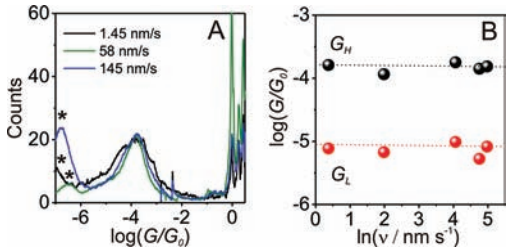

Figure 3. (A) Conductance histograms of **2** constructed from STM-BJ measurements with stretching rates of 1.45 (black), 58 (green), and 145 nm s^{-1} (blue), V_{bias} = 0.1 V. (B) Most probable molecular junction conductances G_H and G_L vs the logarithm of the stretching rate v. The star symbols represent an artifact related to the noise level of our STM-BJ setup.

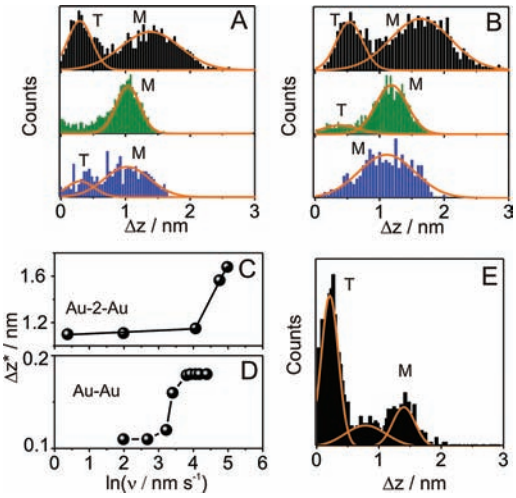

Figure 4. Characteristic lengths distributions for the stretching of molecular junctions of **2** from STM-BJ experiments, and analyzed in the range (A) from $G = 0.7G_0$ to $G = 10^{-5} G_0$ (high-conductance range) and (B) from $G = 0.7G_0$ to $G = 10^{-6} G_0$ (high- and low-conductance range), with stretching rates of 145 (black), 58 (green), and 1.45 nm s^{-1} (blue), V_{bias} = 0.10 V. (C) Most probable characteristic length Δz^{L*} as a function of the stretching rate $\ln v$. (D) Dependence of the characteristic length for the stretching of gold–gold junctions (in $G = 1.1G_0$ to $G = 0.7G_0$) on $\ln v$. The experimental conditions are the same as in panel C. (E) Characteristic length distribution for the stretching of molecular junctions with **2** (in $G = 0.7G_0$ to $G = 10^{-6} G_0$) measured in MCBJ experiments with 2 nm s^{-1}, V_{bias} = 0.1 V.

this point for each individual trace) up to a lower limit G_{min}, typically 1 order of magnitude below the most probable high- (G_H) or low (G_L)-conductance states, respectively. Technical details of this approach were described in our previous publication[62] and are briefly outlined in the SI. Figure 4A,B illustrates distributions of Δz^H and Δz^L determined from all experimental traces as measured at the three different rates v. The distributions show two peaks labeled as T and M. The T peak centered at $\Delta z \approx 0.3$–0.5 nm results from traces showing only through-space tunneling contributions, as verified in experiments with adsorbate-free solutions. The second peak labeled M reflects properties of a "true" molecular junction. The maximum of the M peak as determined by Gaussian fits represents the most probable characteristic distance Δz^* over which a junction can be stretched. With an increase of the stretching rate from 1.45 to 145 nm s^{-1}, Δz^* increases for the high-conductance feature from $\Delta z^{H*} = 0.90$ to 1.50 nm (Figure

dx.doi.org/10.1021/ja211555x | J. Am. Chem. Soc. 2012, 134, 5262–5275

4A). Extending the analysis to the low-conductance region until breakdown is observed, Δz^{L}* ranges from 1.10 to 1.70 nm. The difference Δz^{L}* − Δz^{H}* amounts to ∼0.20 nm and is rather independent of the stretching rate. We also calculated the junction formation probability from the relative areas of the peaks T and M from the displacement histograms in Figure 4B, as defined by Gaussians, and obtained 75%, 85%, and 65% for stretching rates of 1.45, 58, and 145 nm s^{-1}, respectively.

The experimentally observed dependence Δz^{L}* vs ln v for the overall stretching process of **2** (Figure 4C) indicates a thermally activated bond-breaking process.[88−91] The values of Δz^{L}* for **2** and Δz^{Au}* are rather independent of the loading rate below 60 and above 140 nm s^{-1}, which reflects quasi-equilibrium conditions and could be attributed to a spontaneous (due to the thermal fluctuations) or adiabatic (external force that overcomes the binding energy barrier) breakdown regime.[89,90] At intermediate stretching rates, a region of a distinct logarithmic dependence of Δz^{Au}* on ln v is observed. Similar trends were reported before by Huang et al.[89] for the breaking of octanedithiol junctions formed between two gold electrodes. The authors reported values of Δz* = 0.1 and 0.2 nm in the limits of low and high stretching rates, respectively, rather similar to their and our results for the breaking of monatomic gold contacts (Figure 4D). This comparative study let the authors suggest that the breakdown of octanedithiol-based molecular junctions takes place most likely at gold−gold bonds. This hypothesis is supported by single-molecule electromechanical studies using CP-AFM.[92] In case of OPE molecules, the values of Δz^{L}* are distinctly larger (Figure 4C) in the two quasi-equilibrium stretching regimes, as compared to the breaking of a gold−gold atomic contact, but still smaller than the length of the molecule. Clearly, the formation and subsequent breakdown of junctions containing OPE-type molecules involve processes such as picking up the molecule from the surface,[93] coordination and/or conformation changes,[71] and/or sliding along the contacting leads before rupture.[24] Further details will be addressed in the Discussion.

The higher mechanical stability of our MCBJ setup,[73] as compared to a typical STM-BJ experiment (see SI for details), allows resolving simultaneously both quasi-equilibrium states as characterized by a low and a higher characteristic stretching length Δz* (Figure 4E), even at rather low rates of opening/closing the nanocontact junction. The corresponding histograms (see SI) show a clear trend toward a more probable higher characteristic length Δz* with increasing stretching rate.

Current−Voltage Measurements. The high mechanical stability of the MCBJ setup also offers the possibility to acquire simultaneously I−V_{bias} curves during the slow opening and closing of a molecular junction with a typical rate of 0.5 nm s^{-1} (Figure 5). The bias voltage was ramped between −1.00 and +1.00 V at 40 V s^{-1},[73] allowing us to measure 40−50 I−V_{bias} curves per individual trace. The curves measured during the different stages of extension correspond to gold−gold contacts (Figure 5A), molecular junctions (Figure 5B), and the tunneling response through the solvent (Figure 5C). The zero-bias conductances (Figure 5D) were calculated from the slopes of the linear parts of the I−V_{bias} curves in the range from −0.30 to +0.30 V. The 1D log-conductance histogram as constructed from ∼1000 individual data points is displayed in Figure 5E. The estimated most probable junction conductance of **2** in region G_H is in good agreement with data shown in Figure 2E, which supports the reliability of our I−V_{bias} experiments. Sensitivity limitations in the setup for I−V_{bias} measurements at

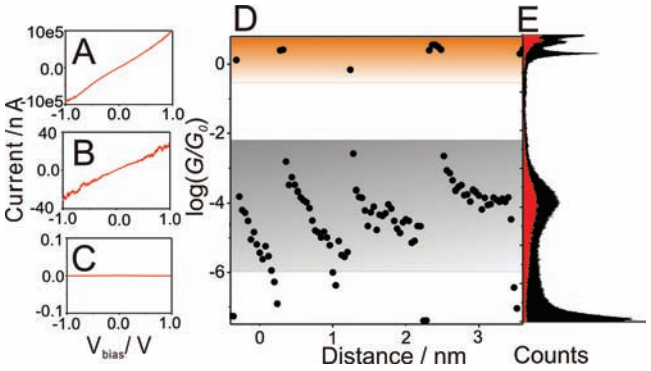

Figure 5. Typical I−V_{bias} curves measured (A) for gold−gold contacts, (B) for molecular junctions and (C) in the tunneling regime during a single stretching trace of **2**, V_{bias} = 0.10 V, pulling rate v = 0.5 nm s^{-1}. (D) Zero-bias conductance as calculated from the slopes of individual I−V_{bias} traces during 4000 stretching sequences. (E) Conductance histograms built from zero-bias conductance of 4000 I−V_{bias} curves (red) and from the conductance−distance traces (black) simultaneously measured with the MCBJ setup.

larger values of V_{bias} prevented us from obtaining reliable data in the G_L region. We also note that some molecular junctions are broken before being completely stretched (examples are the two left traces in Figure 5D), which we attributed to enhanced thermal fluctuations of the junction ("junction heating") at high bias voltages.

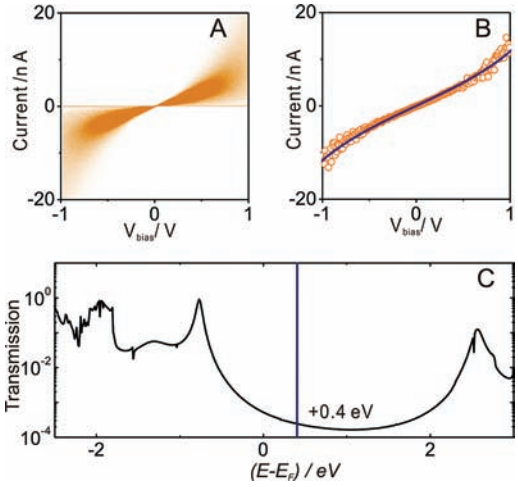

Figure 6. (A) 2D histogram of 4000 I−V_{bias} curves measured for **2** with the MCBJ setup in the high-conductance region of molecular junctions. (B) Statistically significant I−V_{bias} trace (orange dots) calculated from 4000 individual I−V_{bias} curves of **2** and DFT-based I−V_{bias} curve (blue line). (C) Computed transmission trace and SAINT-adjusted value of E_F (for details see Theoretical Methods and SI).

To obtain the most probable I−V_{bias} characteristics of the high-conductance molecular junction, we analyzed statistically the I−V_{bias} curves with zero-bias conductance between 2 × $10^{-5}G_0$ and $10^{-3}G_0$.[73,94,95] Figure 6A shows the 2D I−V_{bias} histogram constructed from 4000 I−V_{bias} traces. For each value of the bias voltage we determined the maximum of the corresponding current distribution (obtained from Gaussians fits) as the most probable current.[73,95] The resulting "statistically significant" I−V_{bias} curve is plotted as orange dots in Figure 6B. The curve shows fluctuations, but no characteristic resonance features. We note that the conductance of molecular

dx.doi.org/10.1021/ja211555x | J. Am. Chem. Soc. 2012, 134, 5262−5275

junctions in the nonresonant tunneling regime is controlled by (i) the position of the dominant transport MO relative to the metal Fermi level and (ii) the broadening of this MO due to the coupling to the metal leads.[5] Comparison of the experimentally most probable $I-V_{bias}$ curve of **2** (dots in Figure 6B) with the computed $I-V_{bias}$ characteristics (blue solid line in Figure 6B), as obtained from ab initio generated transmission curves (SMEAGOL, for details see SI), allowed us to adjust the scale of $E_{HOMO} - E_F$ as obtained from simulations. The current was calculated by integrating the respective transmission curve in the corresponding bias window. The Fermi level that gave the best agreement was slightly higher in energy (0.4 eV, blue vertical line) than the original Fermi level.

The agreement is rather good despite the fact that nonequilibrium effects, such as the movement of resonances under an applied bias voltage, were not taken into account (these and other effects, such as bias-induced destruction of resonances, start to dominate at higher voltages). The $I-V_{bias}$ curve is typical of a system with the Fermi level in the HOMO−LUMO gap and close to a resonance; i.e., the current is ohmic at low voltages but changes its slope and increases more sharply at higher voltages. Figure 6C illustrates the SAINT-corrected transmission curve (see SI for more details), which demonstrates that the resonance closest to the Fermi level E_F in the modified energy scale represents a HOMO feature, indicating that HOMO-mediated hole transport is likely to dominate the transport behavior of **2** attached to two gold leads. This conclusion is in agreement with previous work on dithiol-terminated OPE rods attached to gold leads[53] and is directly supported by thermopower measurements in phenyl-dithiol-containing heterojunctions.[96]

Effect of Molecular Structure on Conductance. *The Most Probable Conductance.* Following the experimental approaches and data analyzing strategies introduced for the reference compound **2**, we designed and characterized 11 dithiol-terminated OPE-type molecules with varied length, HOMO−LUMO energy, and conjugation of the π-system. We take the distance between two sulfur atoms obtained from DFT calculations of the relaxed extended molecules (see Theoretical Methods and Table S2 in SI for details) as a transport-relevant molecular length, L_m. The values of L_m range between 1.32 (**1**) and 3.39 nm (**11**). The HOMO−LUMO gap was estimated experimentally from UV/vis absorption spectra of the *tert*-butyl-terminated dithiols. All compounds are fully π-conjugated, except the anthraquinone-based cross-conjugated compound **8** and the dehydroanthraquinone derivative **9** with broken π-conjugation. Tables S1 and S2 (SI) summarize characteristic geometric and energetic parameters of these molecules.

In the following we discuss key experimental results obtained with a stretching rate of either 58 (STM-BJ) or 2 nm s^{-1} (MCBJ). These rates ensure that all experiments are carried out in the "quasi-equilibrium" region of the spontaneous breakdown (cf. Figure 4). Original data for all investigated compounds are given in the SI.

Figure 7 displays the 1D log-conductance histograms for 10 compounds. Figure 8A and Table S3 (SI) summarize all characteristic conductance data. The data plotted in Figure 7A demonstrate that the main conductance features of G_H type shift to lower values with increasing molecular length. In particular, the most probable conductance decreases from 1.46 × $10^{-3}G_0$ (**1**) to $10^{-6}G_0$ (**11**). Comparing the data for compound **2** and the molecular wires included in Figure 7B

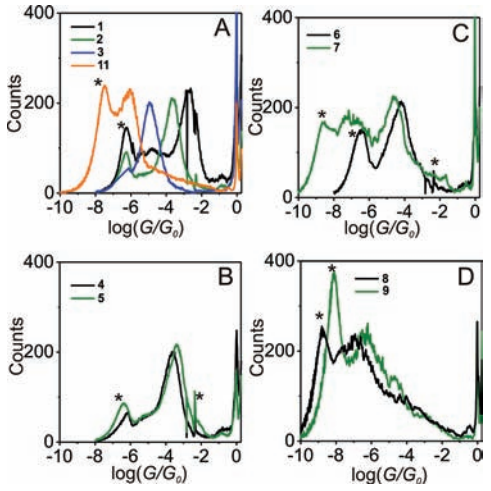

Figure 7. 1D conductance histograms of **1**−**9** and **11**, measured in the STM-BJ setup (**1**−**6**) or the MCBJ stage (**7**−**9**, **11**), at V_{bias} = 0.1 V. The STM-BJ- and MCBJ-generated histograms are both based on the analysis of 2000 individual traces.

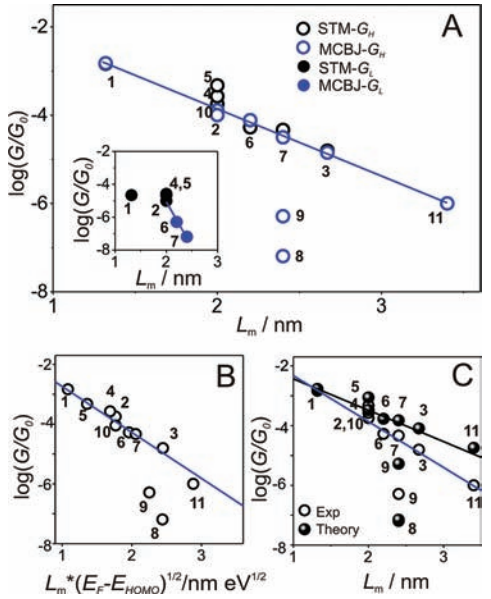

Figure 8. (A) Experimental conductances G_H and G_L as a function of the molecular length L_m (the inset shows the low-conductance G_L as a function of L_m). (B) High-conductance G_H plotted vs $L_m(E_F - E_{HOMO})^{1/2}$. (C) DFT-based G_H values (black circles and black line) as a function of L_m. For comparison, also the experimental values are given as open circles and blue line. The numerical conductance values and molecular lengths are summarized in Tables S2 and S3 (SI). Computational details are given in the Theoretical Methods section and in the SI.

reveals a similar trend with increasing HOMO−LUMO gap. Nearly identical most probable conductance data were obtained in the STM-BJ and the MCBJ experiments, except for wires **6**−**9** and **11**. Reliable data for these molecules were accessible only in the MCBJ configuration because of sensitivity limitations of the STM setup in the low-bias regime. Compounds **2** and **10** gave identical results, suggesting that the hexyloxy substitution of the central phenyl rings has no significant effect on the transport close to the Fermi level. This hypothesis is supported by DFT calculations reported by Martin et al.[87]

dx.doi.org/10.1021/ja211555x | J. Am. Chem. Soc. 2012, 134, 5262−5275

Comparing our results in the high-conductance region G_H to those reported by other authors reveals that our values for **1** and **5** are much higher ($1.46 \times 10^{-3} G_0$ vs $0.54 \times 10^{-4} G_0$ by Beebe et al.[34]) or lower ($0.47 \times 10^{-3} G_0$ vs $7.7 \times 10^{-3} G_0$ by Reichert et al.[42]). These differences may be partially related to the different experimental techniques used as well as to environmental conditions chosen. The situation is more consistent with dithiolated OPE derivatives with three coupled phenyl rings, such as **2** and **10**, where conductances ranging between $5.0 \times 10^{-5} G_0$ and $1.8 \times 10^{-4} G_0$ were published.[44,45,50−52,85] Comparing further the dithiol-terminated wires **1** and **2** with the corresponding diamines[47,51,95] shows higher single-junction conductance data for the dithiol derivatives. The same trend was also found for substituted benzene and biphenyl derivatives.[48,50,58,63,97] Lu et al. reported the opposite for oligo(*p*-phenylene-ethynylene) rods with more than three phenyl rings, based on a combined STM-BJ and CP-AFM study.[51] These authors attributed their observations to an intrinsic change of the transport mechanism from tunneling to hopping.

Figure 8 summarizes the dependencies of the most probable conductances G_H (high) and G_L (low) versus the molecular lengths L_m. The analysis of the high-conductance state G_H of the single molecular junctions formed by the linearly conjugated compounds **1**−**3**, **6**, **7**, **10**, and **11** demonstrates an exponential distance dependence with a decay parameter $\beta_{GH} = 3.4 \pm 0.1$ nm^{-1}. No indication for a change of the transport mechanism from tunneling to hopping, as recently discussed for a series of diamino-substituted OPE derivatives, was found.[51] By extrapolating the G_H versus L_m dependence to $L_m = 0$, we determined an effective contact resistance for two Au−S bonds equal to 80 kΩ, or 40 kΩ per Au−S site. This value is in agreement with literature data reported for Au−dithiolate−Au junctions.[57,98]

Furthermore, extrapolation to $L_m = 0.619$ nm, the S−S distance in benzenedithiol, yields a conductance of $0.012 G_0$, in good agreement with literature data.[2,50,86,97] The value of β_{GH} found in our study is identical to those reported in electrochemical electron transfer experiments with ferrocene-terminated OPE wires by Creager et al.[40] and Newton et al.,[39] and larger than those determined in CP-AFM experiments (2.1 nm^{-1} by Liu et al.[33]) as well as for OPEs with amine anchoring groups (2 nm^{-1} by Lu et al.[51]) and carbodithiolate linkers (0.5 nm^{-1} by Xing et al.[50]). Tomfohr et al.[99] analyzed electron transport in OPE-type oligomers on the basis of a Landauer formalism in combination with a band structure analysis and obtained $\beta_{th} = 2.3$ nm^{-1} for a planar conformation. These authors also demonstrated that β_{th} increases with increasing torsion angle between adjacent phenyl rings.

The decay parameter β_{GH} obtained in this experimental OPE study compares with that of other typical molecular bridges as follows: saturated alkanes[57,70,71] (7−10 nm^{-1}) > oligophenyls[100,101] (PP, 3.5−5 nm^{-1}) > OPE (this work) > oligo(phenylene-vinylenes)[39,57] (OPV, 1.7−1.8 nm^{-1}) > oligothiophene[61] (OT, 1 nm^{-1}) > oligoynes[59] (OY, 0.6 and 0.06 nm^{-1}). This trend reflects an enhanced electronic communication across the molecular bridge with increasing delocalization of the adjacent π-system and lowering of the HOMO−LUMO gap.[39]

We also note that molecules having the basic motif of compound **2** with a fixed S−S distance but varying in the structure of the central aromatic core, such as **2**, **4**, and **5**, lead to a decrease of the HOMO−LUMO gap (Tables S1 and S2) in the sequence **2** > **4** > **5**. Figures 7B and 8A demonstrate a monotonic increase of the most probable conductances with decreasing HOMO−LUMO gap.

Molecules **4** and **5** thus do not follow the general G_H vs L_m trend displayed as the blue line in Figure 8A. The latter, however, is only a part of the more general dependence that can be expressed by the equation for tunneling over a distance L through a rectangular energy barrier with the height Φ (in the low bias limit):[102]

$$G \approx \exp(-10.12\ \text{nm}^{-1}\ \text{eV}^{-1/2} \sqrt{\Phi} L) \quad (1)$$

For the through-molecule tunneling we attribute the tunneling distance L to the molecular length L_m, and the energy barrier Φ to the difference between the Fermi energy of the gold electrodes E_F and the energy of the closest molecular orbital. The simulations of charge transport in various molecules bound via thiol anchors to gold electrodes demonstrate unequivocally that the transport proceeds by HOMO-assisted hole-tunneling (see also Theory section).[5] Consequently, we set $\Phi = E_F - E_{HOMO}$.[50,52] We estimated the values of E_{HOMO} by using DFT calculations. However, since DFT underestimates the HOMO−LUMO gap, the energy levels were adjusted on the basis of UPS measurements of the respective anthraquinone derivatives (see SI for details). E_F = 5.0 eV was taken from the work reported by Veenstra et al.[103]

To consider both the length and the influence of the tunneling barrier, we replotted the $\log(G_H/G_0)$ data of all 11 compounds versus $L_m(E_F - E_{HOMO})^{1/2}$ (Figure 8B). Except for **8** and **9**, the data points of the nine fully conjugated OPE analogues display a clear linear dependence. The fit is represented by the blue line in Figure 8B. Thus, the simple tunneling eq 1 containing both the energetic and the geometric parameters describes the conductance variation. There are, however, deviations from this linear behavior.[104] In particular, compounds **8** and **9** have the same "skeleton" as **7**, but a different electronic structure. The conductance of **9** is lower than that of **7** due to the broken π-conjugation in the center of the molecule, which cannot be accounted for just by the variation of the HOMO level. The cross-conjugated anthraquinone-based compound **8** has an even lower conductance. Thygesen et al.[105,106] demonstrated in recent simulation studies that the cross-conjugation in **8** results in a destructive quantum interference effect, leading to a sharp drop in the transmission probability of the electrons at the Fermi energy.[106]

The inset in Figure 8A also shows the length dependence of the most probable conductances G_L in the low-conductance region. This conductance feature was observed for six compounds only. While the conductances for the shorter molecular wires **1**, **2**, **4**, and **5** vary only slightly from $10^{-5} G_0$ (**2**) to $2.6 \times 10^{-5} G_0$ (**4**), a strong decrease is observed for the fused linearly conjugated rods **6** and **7**. The absence of the G_L feature for the compounds **3** and **11** might reflect the additional conformation degrees of freedom due to phenyl ring rotations[99] as well as the steric influence of the hexyloxy substituents in the latter molecule. The second distance decay parameter determined for compounds **2**, **6**, and **7** (inset in Figure 8A) amounts to $\beta_{GL} = 14.6 \pm 0.35$ nm^{-1}, which is significantly larger than β_{GH} as well as decay parameters for other typical molecular bridges reported so far.

2D Histograms, Stretching Length, and Tilt Angle. Inspection of the 2D conductance−displacement histograms reveals a slight but distinct decrease of the conductance during the stretching for all investigated compounds (see Figure 2 and

Figures S7–S19, SI). For compounds **1**, **2**, **4**–**7**, and **10**, a second feature with lower conductances evolves in experiments carried out in TMB/THF. The feature is even more pronounced when decane is used as a solvent, and when working with deprotected molecules. The possible origin of the low-conductance feature will be addressed further.

Following the strategy presented above for compound **2**, we analyzed the characteristic length distributions upon stretching in the high-conductance range, and up to the low-conductance region. They were defined as distances over which the tip moves while the junction conductance drops from $0.7G_0$ to $0.1G_H$ for Δz^H or from $0.7G_0$ to the noise level ($10^{-6}G_0$ for STM-BJ and $10^{-8}G_0$ for MCBJ measurements) for Δz^L. Pulling rates of 58 and 2 nm s^{-1} were employed in STM-BJ and MCBJ experiments, respectively.

All length distribution histograms for compounds **1** and **3**–**11** are presented in the SI. The most probable characteristic lengths Δz^{H*} and Δz^{L*} increase with molecular length L_m (Table S3). For experiments with two conductance features resolved, the difference $\Delta z^{L*} - \Delta z^{H*}$ amounts to 0.20–0.35 nm rather independently of molecule and solvent. This value is close to the diameter of a gold atom and might indicate that the pulling of an additional gold atom is involved in the junction transition from the high to the low-conductance state.

In order to estimate the absolute distances between the two gold electrodes in the most probable configurations prior to breaking, we need to consider the "snap-back", i.e., the fast relaxation of gold electrodes upon breaking a monatomic gold–gold contact. This effect is in particular responsible for the sharp decrease of the current from $\sim 1G_0$ into the molecular conductance region. To estimate the snap-back distance, we extrapolated the tail of the tunneling current measured after breaking the gold–gold contact to G_0. We obtained a distance correction Δz_{corr} = 0.5 nm (for further details see SI and refs 24, 83, and 107). Figure 9A,B illustrates the snap-back-corrected characteristic lengths for the high and for the low-conductance states, $z^{H*} = \Delta z^{H*} + \Delta z_{corr}$ and $z^{L*} = \Delta z^{L*} + \Delta z_{corr}$, as a function of L_m. z^{H*} is smaller than L_m for all molecules investigated. On the other hand, the snap-back-corrected electrode separation in a completely stretched junction, $z^{L*} = \Delta z^{L*} + \Delta z_{corr}$, is not always smaller than L_m (cf. molecules **1**, **4**, and **5**, Figure 9B and Table S3).

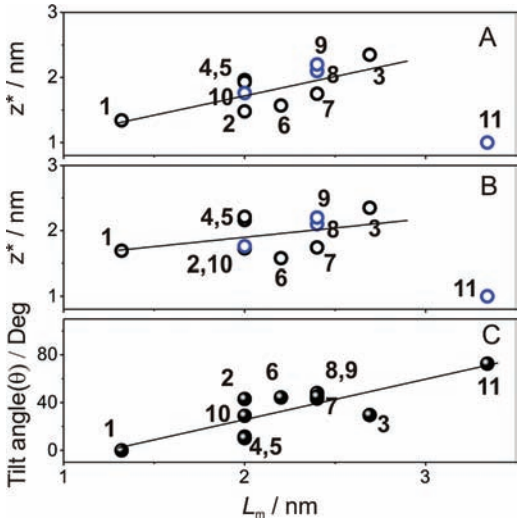

Figure 9. Most probable characteristic length data z^* as extracted from the analysis of STM-BJ (black circles) and MCBJ (blue circles) data of **1** to **11** in the conductance ranges (A) $0.7G_0 < G < 0.1\ G_H$ (z^{H*}, A) and (B) $0.7G_0 < G < 10^{-6}G_0$ (STM-BJ experiments) or $0.7G_0 < G < 10^{-8}G_0$ (MCBJ experiments) (z^{L*}, B). (C) Tilt angle θ of molecules **1**–**11** in the high-conductance state prior to contact breaking as a function of the molecular length.

We used z^{H*} to estimate the tilt angle θ of the molecules in the high-conductance state (vs the normal to electrode surface) from the simple geometric relation $\theta = \arccos(z^{H*}/L_m)$. The results are presented in Figure 9C. They demonstrate that θ increases with L_m. The tilt angle is zero for **1**, indicating that the molecule is in an upright position in the high-conductance state, while longer molecules are inclined. This observation also suggests that the longer OPE wires most probably slide along the gold contacts upon formation of a single molecular junction, and breaking occurs, even under conditions of a maximum possible stretching, not in a fully upright position but at an angle to the surface normal (see Table S3).

Finally we would like to comment on the origin of the low-conductance features. They have rather peculiar properties: (i) They were observed as shoulders and low-density clouds in the conductance histograms only for 6 compounds out of 11. (ii) They are more pronounced in decane than in TMB. (iii) The conductances G_L are independent of molecular length for the short molecules, and for long molecules they decrease with a distance decay parameter being higher than that for any type of molecular bridge studied so far (including aliphatic wires). (iv) For some molecules the electrode separation in the low-conductance state is longer than the molecular length L_m. We can account for these trends only by attributing the low-conductance features to the conductance through π–π-stacked molecules.[45,53] Stacking is particular promoted by the higher density of π-electrons, as in compounds **4**–**7**, which indeed show low-conductance features, as well as by nonaromatic solvents. However, the low-conductance feature for the π-electron-deficient molecule **1** may as well be accompanied by the pulling out of a gold atom from the tip or the surface.

Ab Initio Transport Calculations for the Three Series of Molecules. To provide further insight into the experimentally observed trends and the evolution of the molecular junctions formed between the various OPE derivatives coupled to gold electrodes, we performed theoretical calculations using a combination of DFT and a nonequilibrium Green's functions formalism (for further details see SI).

The STM-BJ configuration was represented by an extended molecule with one surface atom bound to a three-fold hollow (H) site of the Au(111) surface (Au–S distance ~0.21 nm) and the other one to a gold adatom, which was contacted to the surface in a H site (Au–S distance ~0.24 nm) following the (111) direction of growth (see Figure S20). This geometry was found to be energetically the most stable on the basis of LDA calculations.[52,53] We also considered adatom–adatom (A-A), hollow–hollow (H-H), and top-top (T-T, not shown) geometries as well as the role of the tilt angle θ of the molecular axis to the surface normal and the torsion angle φ upon rotation of the central phenyl ring. Figure 10 illustrates selected configurations (for further details see SI). We computed the energy-dependent transmission $T(E)$ using the ab initio code SMEAGOL[75,76] for the description of the electron transport in various "extended molecule" configurations. $T(E)$ represents the probability for electrons injected with an energy E from one electrode to be transmitted through

dx.doi.org/10.1021/ja211555x | J. Am. Chem. Soc. 2012, 134, 5262–5275

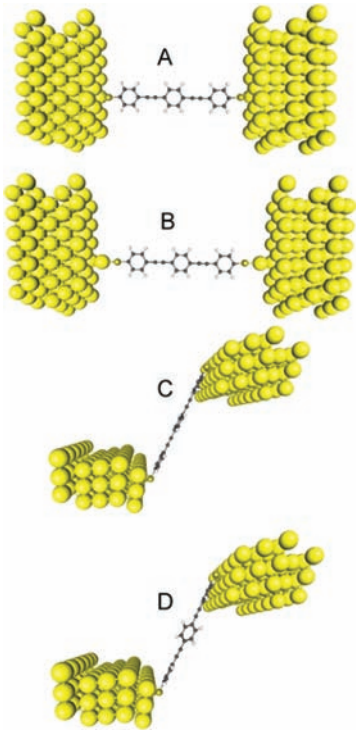

Figure 10. Four representative configurations of the extended molecule used in the calculations: side views of (A) hollow−hollow (H-H) and (B) adatom−adatom (A-A) and (C) top view of H-H with a tilt angle of 80° with respect to the normal to the surface. (D) The same configuration as in (C), but with a torsion angle of 38° of the central ring.

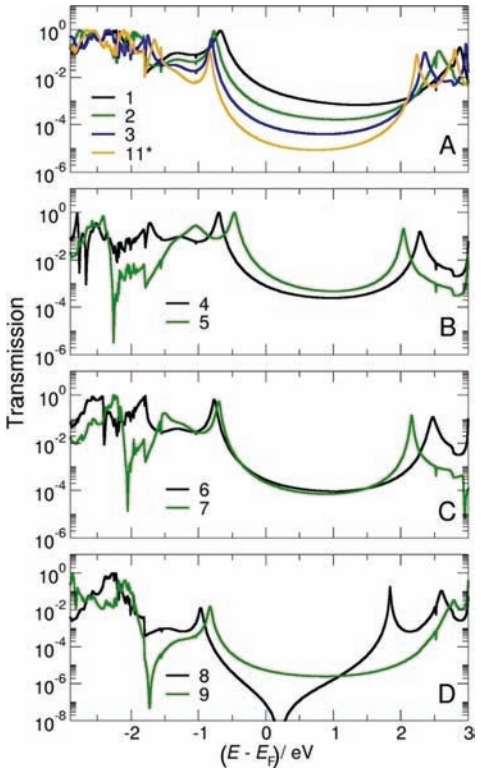

Figure 11. SAINT-corrected transmission curves calculated with SMEAGOL for **1**−**9** and **11**. The hexoxy-side groups in **11** were not included into the calculations.

the molecular junction. The conductance G is defined as the transmission $T(E_F)$ evaluated at the Fermi level E_F in units of the conductance quantum G_0. Molecular states of the OPEs appear as resonance peaks in the transmission spectrum.

Qualitative trends in families of molecules are known to be correctly reproduced by transport calculations based on bare DFT-derived mean-field Hamiltonians. However, quantitative agreement between experiment and theory is hampered by the bandgap problem (DFT underestimates the HOMO−LUMO gap) and other problems related to the LDA functional, such as self-interaction errors.[78,108]

In the bare DFT calculations of the family of the linearly conjugated OPE derivatives **1**−**11**, the Fermi level is found to be typically pinned to the HOMO orbital, so that the conductance at E_F is overestimated. To resolve this problem, a semiempirical self-energy and screening energy correction has been introduced by a scissor-like operator (spectral adjustment in nanoscale transport, SAINT)[79−81] prior to the transport calculations.

The SAINT operator moves the occupied molecular levels (HOMO) to lower and the unoccupied levels (LUMO) to higher energies, respectively. The derived mean-field Hamiltonian was constructed in such a way that (i) the HOMO agrees with UPS experiments of OPE derivatives attached to gold films and (ii) that the HOMO−LUMO gap matches the optical HOMO−LUMO gaps, which were estimated from the onsets of the UV/vis absorption spectra (Table S1). Figure 11 shows plots of the SAINT-corrected transmission curves of **1** to **11** for the adatom−hollow (A-H) upright geometry. The resonance closest to the Fermi level (about 1 eV lower than E_F) corresponds to a HOMO feature indicating a HOMO-mediated hole transport behavior in all wires. The relative position of $(E_{HOMO} - E_F)$ upon the SAINT correction is in good agreement with the estimated shift, based on the analysis of the experimentally obtained $I-V_{bias}$ characteristics in the molecular plateau region (Figure 6).

The transmission coefficients $T(E)$ of **1**−**3** and **11** (and **10**, which is not shown) reveal that as the length increases, the HOMO−LUMO gap decreases (Figure 11A), since for longer molecules the electrons can more easily delocalize along the molecule backbone and the repulsion between levels decreases. At the same time the transmission $T(E_F)$ at the Fermi energy $(E = E_F)$ near the middle of the gap decreases exponentially. This second effect dominates the decrease in the HOMO−LUMO gap and produces an exponential reduction of the transmission near the HOMO resonance, in agreement with the experimental results (cf. Figure 8A).

Comparing molecules **2**, **4**, and **5** (Figure 11A,B) reveals a decrease of the HOMO−LUMO gap due to an increase of the electron delocalization in the central aromatic moiety, which decreases the separation between levels. In this case $T(E_F)$ does not decrease exponentially, since all molecules have roughly the same length (Tables S1 and S2). The net effect is therefore an increase of the $T(E_F)$ due to the presence of the nearby HOMO resonance.

In the series of molecules **2**, **6**, and **7**(Figure 11A,C) both the reduction of the HOMO−LUMO gap and the increase of the molecular length are important. The LUMO shifts downward and the conductance in the gap decreases exponentially. As a consequence $T(E_F)$ decreases slightly from **2** to **6** to **7**.

We have plotted in Figure 8C the zero-bias conductance, as calculated from the SAINT-corrected transmission at the Fermi level, as a function of the molecular length. The graph

dx.doi.org/10.1021/ja211555x | J. Am. Chem. Soc. 2012, 134, 5262−5275

demonstrates that the experimental trend is correctly reproduced by the theoretical calculations. More importantly, the quantitative zero-bias conductance values are also close to the experimental values, which is not typical of DFT-based calculations without corrections. In addition, the decay constant obtained for series **1**−**3**, **6**, **7** (and **11**) is 2.76 nm $^{-1}$, in good agreement with the experimental value 3.4 nm^{-1}. We note that the calculation of **11** was carried out without incorporating the hexyloxy-substituents, which are considered to have a negligible effect on the transport close to the Fermi level, as it was shown recently for methoxy and *tert*-butyl substitutions in OPEs.[53] Additional calculations following the same strategy as outlined above reveal that the H-H configuration leads to similar conclusions, however with higher junction conductances. The lowest overall conductances were found for the A-A coordination geometry (shown in SI). The best agreement between experimental and computed data in the high-conductance range G_H was obtained for the A-H configuration, which may be also considered as a reasonable representation of the STM-BJ geometry. However, contributions of other Au−S coupling configurations including those of "phase-on" edge sites during the evolution of the molecular junction between the gold leads and the dithiolated OPE-type molecules cannot be excluded,[53,63,71,109,110] as the 1D and 2D conductance histograms show a non-negligible width in the distribution around the most probable conductance values (Figure 2 and SI). Finally, we comment that the distinct deviations of **8** and **9** from the length-dependence trend of the OPE wires investigated could be attributed to the relatively high position of the LUMO level resulting from the broken π-conjugation in **9** and the appearance of a destructive quantum interference in **8** as demonstrated in recent studies[10S,106,111,112] and by the transmission curves plotted in Figure 11D. Thygesen et al. demonstrated that the quantum interference effect is rather insensitive to details of the contact geometry. It is a property of the symmetry of the molecular orbitals and, as a consequence, its overall appearance is not severely influenced by the exact position of the HOMO and LUMO levels, respectively. $T(E_F)$ is predicted to show without and with the application of a scissors operator, such as in the SAINT correction used in our approach, a distinct minimum leading to a conductance at E_F which is much smaller than that for the "simple" anthracene rod **7**. This trend is indeed observed experimentally (see Figure 8A).

Despite the success, there are however unresolved questions related to the evolution of the conductance with the stretching distance between the STM tip and the surface. From the 2D conductance ($\log(G/G_0)$) versus displacement (Δz) histograms (Figure 2 and SI), it is clear that as Δz increases, the high-conductance G_H portion of the histogram decreases toward lower values. Furthermore, the relative distance at which this region terminates is smaller than L_m, the length of the molecule. Figure 9A,B illustrates that this trend is valid for the most probable characteristic length in the high- (z^{H*}) as well as in the low-conductance range (z^{L*}), with corrections for the snap-back distance Δz_{corr} = 0.5 nm. Figure 9C shows that the tilt angles of the molecular in the junction in the high-conductance state are increasing with increasing molecular length L_m. These experimental results imply that the OPE wires are tilted with respect to the surface, and that the angle θ relative to the surface normal decreases as the tip retracts. Therefore we also carried out calculations with a rather large angle for the prototype wire **2**. We found that the transmission is sensitive to θ, and increases significantly for large angles. (A similar trend was proposed by Haiss et al.[52]) These results are illustrated in Figure 12. The behavior can be explained by

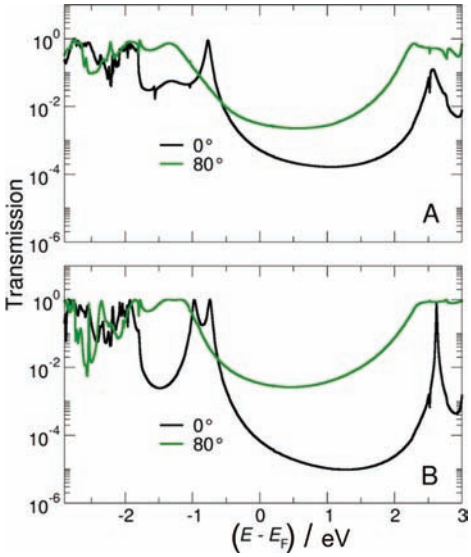

Figure 12. SAINT-corrected transmission curves obtained for molecule **2** in (A) a straight (0°) and tilted (80°) in A-H configuration and (B) an A-A configuration.

considering that the main orbitals on the sulfur that contribute to the HOMO resonance and couple to the π-orbitals in the carbon backbone (x and y p-orbitals) have by symmetry zero overlap with the s-orbital of the gold adatom (tip) or the hollow site atoms (substrate), and a very small overlap with the more localized d-orbitals when the molecule is straight.[113−115] Therefore, they give a very small coupling. When the molecule is rotated, however, such orbitals become nonorthogonal with the gold orbitals and increase the overlap. This effect enhances the coupling, or in other words, increases the density of states at E_F, as can be seen in the dramatic increase of the width of the HOMO resonance when the angle increases (Figure 12).

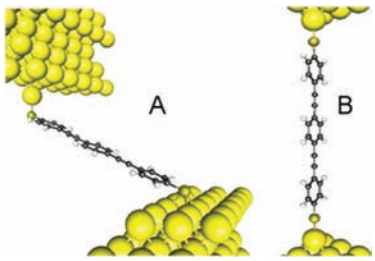

Figure 13. Summary of the entire stretching process, with the two limiting configurations: (A) tilted molecule connected in an A-H configuration at the beginning and (B) a straight molecule connected in an A-A configuration at the end of the stretching process.

From the experimental observation of tilt angles and characteristic lengths (z^{H*}, z^{L*}), we can draw the following picture of the evolution of the junction as the tip is retracted from the surface (Figure 13). For small relative distances Δz, the OPEs typically have a large tilt angle θ with respect to the surface normal, which is basically determined by the snap-back distance of $\Delta z_{corr} \approx 0.5$ nm. As Δz increases, the most probable value of θ and the most probable conductance decrease. At

dx.doi.org/10.1021/ja211555x | J. Am. Chem. Soc. 2012, 134, 5262−5275

intermediate distances, a range of angles are encountered, leading to a spread of conductance values of the junctions. We also note that fluctuations of the torsion angle φ between the phenyl rings could add to the spread in the main conductance region G_H (see SI for transmission curves). Upon further displacement, typically $(z^{H*} - z^{L*}) = 0.2-0.3$ nm, several OPE wires (**1**, **2**, **4**−**7**) show clear evidence for the evolution of a low-conductance region G_L on the right of the main conductance region in the 2D conductance histograms (see SI). For molecule **1**, θ is estimated to be zero, which indicates that the molecule is completely elongated in the junction. The probability of forming $\pi-\pi$-stacks in the molecular junction is rather low for **1** due to the low π-electron density in the molecule. Further, based on the snap-back-corrected characteristic length z^{L*}, it is clear that the low-conductance feature observed in the histogram can be attributed to the pulling out of a gold atom from the electrode. This case would correspond to the molecule also coupled to an adatom on the surface, whose presence would give a longer distance relative to the surface normal and a lower conductance when the molecule assumes small angles. Indeed the difference in conductance between the A-H and the A-A configurations is close to the experimentally observed trends. Note, however, that the results are rather similar to those of the A-H configuration when the angles are large, which seems to indicate that such angles are not favored in this configuration and at those distances. The two limiting configurations of the pulling process are displayed in Figure 13, namely the A-H with a tilt angle and the straight A-A, which give rise to the highest and the lowest values of conductance, respectively. Molecules **4**−**7** contain larger π-electron cores, which can facilitate $\pi-\pi$-stacking. For these molecules there is a high probability to form supramolecular $\pi-\pi$-stacking junctions, which may represent the low-conductance state. Comparative experiments of mono- and dithiolated OPE rods suggest that supramolecular $\pi-\pi$-stacks could form indeed.[44,52] Both modes, the A-A configuration as well as the intermolecular $\pi-\pi$-stacking, may represent the final stage of molecular junction breakage, or may occur even coupled.

CONCLUSIONS

We studied experimentally (STM-BJ and MCBJ techniques) and theoretically the conductance of a family of OPEs with thiol linker groups. 1D and 2D conductance histograms showed well-defined conductance features of the junctions formed. We observed experimentally and theoretically that the junction conductance decreases with molecular length and increases with a decrease in $(E_F - E_{HOMO})$, the difference between E_F and the nearest molecular orbital, which is E_{HOMO} in the present case. The exponential decay of the conductance with molecular length and the value of the decay constant β indicate that the charge transport through these molecules follows a nonresonant tunnelling mechanism. The SAINT-corrected DFT calculations with a adatom−hollow contact geometry for the high-conductance state G_H show an excellent agreement with the experiment, both qualitatively and quantitatively. We also conclude that the most probable breaking event of a stretched molecular junction occurs in a tilted geometry. Distinct deviations from the experimental correlation of conductance versus distance L_m for the cross-conjugated wire **8** and OPE **9** are attributed to a destructive quantum interference and to the broken π-conjugation, respectively.

Experimentally we found high (G_H) and low (G_L)-conductance values for the OPEs **1**, **2**, **4**−**7**. Theoretical calculations suggest that the appearance of the low-conductance feature originates from a change in surface coordination from a adatom−hollow to an adatom−adatom geometry with the molecular rod assuming a straight orientation to the surface normal for smaller molecules (**1**, **2**). The involvement of stacking interactions in this mechanism cannot be excluded for the molecules with larger π-electron core (**4**−**7**), and are one of the targets of our current work.

In summary, we have developed, employing a combined experimental and theoretical approach, a rather uniform description of the formation and breaking of OPE-type molecular rods attached to gold electrodes. We demonstrated the sensitivity of our complementary STM-BJ and MCBJ approach, and developed clear correlations between molecular structure features and conductance, which shall serve as a guidance for future research on designing and developing nanoscale-based molecular circuits.

ASSOCIATED CONTENT

Supporting Information

Details on the molecular synthesis, the experimental setup, and data analysis as well as the DFT-type transport calculations. This material is available free of charge via the Internet at http://pubs.acs.org.

AUTHOR INFORMATION

Corresponding Author

j.c.hummelen@rug.nl; c.lambert@lancaster.ac.uk; thomas.wandlowski@dcb.unibe.ch

Author Contributions

⊗These authors contributed equally to this work.

Notes

The authors declare no competing financial interest.

ACKNOWLEDGMENTS

This work was supported by the Swiss National Science Foundation (200021-124643; NFP 62), EC FP7 ITN "FUNMOLS" Project No. 212942, DFG under SPP 1243, and the University of Bern. The authors thank I. Pobelov and A. Mishchenko for discussions and critical reading of the manuscript, and Prof. S. Höger for providing molecules **10** and **11**. H.V. acknowledges NanoNed, funded by the Dutch Ministry of Economic Affairs (project GMM. 6973). V.M.G.-S. thanks the Spanish Ministerio de Ciencia e Innovación for a Ramon y Cajal Fellowship (RYC-2010-06053) and the project FIS2009-07081.

REFERENCES

(1) Aviram, A.; Ratner, M. *Chem. Phys. Lett.* **1974**, *29*, 277−283.
(2) Chen, F.; Hihath, J.; Huang, Z. F.; Li, X. L.; Tao, N. J. *Annu. Rev. Phys. Chem.* **2007**, *58*, 535−564.
(3) McCreery, R. L.; Bergren, A. J. *Adv. Mater. (Weinheim, Ger.)* **2009**, *21*, 4303−4322.
(4) Moth-Poulsen, K.; Bjornholm, T. *Nat. Nanotechnol.* **2009**, *4*, 551−556.
(5) Cuevas, J. C.; Scheer, E. *Molecular Electronics: An Introduction to Theory and Experiment*; World Scientific: Singapore, 2010.
(6) van der Molen, S. J.; Liljeroth, P. *J. Phys.: Cond. Matt.* **2010**, *22*, 133001−133030.
(7) Li, C.; Mishchenko, A.; Pobelov, I.; Wandlowski, T. *Chimia* **2010**, *64*, 383−390.

(8) Nichols, R. J.; Haiss, W.; Higgins, S. J.; Leary, E.; Martin, S.; Bethell, D. *Phys. Chem. Chem. Phys.* **2010**, *12*, 2801−2815.
(9) Metzger, R. M. *Unimolecular and Supramolecular Electronics II*; Topics in Current Chemistry *313*; Springer Verlag: Berlin, 2012.
(10) Tao, N. J. *Nat. Nanotechnol.* **2006**, *1*, 173−181.
(11) Song, H.; Reed, M. A.; Lee, T. *Adv. Mater. (Weinheim, Ger.)* **2011**, *23*, 1583−1608.
(12) Weibel, N.; Grunder, S.; Mayor, M. *Org. Biomol. Chem.* **2007**, *5*, 2343−2353.
(13) Tour, J. M. *Chem. Rev.* **1996**, *96*, 537−553.
(14) Díez-Pérez, I.; Hihath, J.; Lee, Y.; Yu, L. P.; Adamska, L.; Kozhushner, M. A.; Oleynik, I. I.; Tao, N. J. *Nature Chem.* **2009**, *1*, 635−641.
(15) Metzger, R. M.; Chen, B.; Hopfner, U.; Lakshmikantham, M. V.; Vuillaume, D.; Kawai, T.; Wu, X. L.; Tachibana, H.; Hughes, T. V.; Sakurai, H.; Baldwin, J. W.; Hosch, C.; Cava, M. P.; Brehmer, L.; Ashwell, G. J. *J. Am. Chem. Soc.* **1997**, *119*, 10455−10466.
(16) Elbing, M.; Ochs, R.; Koentopp, M.; Fischer, M.; von Hanisch, C.; Weigend, F.; Evers, F.; Weber, H. B.; Mayor, M. *Proc. Natl. Acad. Sci. U.S.A.* **2005**, *102*, 8815−8820.
(17) Song, H.; Kim, Y.; Jang, Y. H.; Jeong, H.; Reed, M. A.; Lee, T. *Nature* **2009**, *462*, 1039−1043.
(18) Xu, B. Q.; Xiao, X. Y.; Yang, X. M.; Zang, L.; Tao, N. J. *J. Am. Chem. Soc.* **2005**, *127*, 2386−2387.
(19) Lortscher, E.; Ciszek, J. W.; Tour, J.; Riel, H. *Small* **2006**, *2*, 973−977.
(20) Green, J. E.; Choi, J. W.; Boukai, A.; Bunimovich, Y.; Johnston-Halperin, E.; DeIonno, E.; Luo, Y.; Sheriff, B. A.; Xu, K.; Shin, Y. S.; Tseng, H.-R.; Stoddart, J. F.; Heath, J. R. *Nature* **2007**, *445*, 414−417.
(21) Lee, J.; Chang, H.; Kim, S.; Bang, G. S.; Lee, H. *Angew. Chem., Int. Ed.* **2009**, *48*, 8501−8504.
(22) Blum, A. S.; Kushmerick, J. G.; Long, D. P.; Patterson, C. H.; Yang, J. C.; Henderson, J. C.; Yao, Y. X.; Tour, J. M.; Shashidhar, R.; Ratna, B. R. *Nat. Mater.* **2005**, *4*, 167−172.
(23) Choi, B. Y.; Kahng, S. J.; Kim, S.; Kim, H.; Kim, H. W.; Song, Y. J.; Ihm, J.; Kuk, Y. *Phys. Rev. Lett.* **2006**, *96*, 156106.
(24) Quek, S. Y.; Kamenetska, M.; Steigerwald, M. L.; Choi, H. J.; Louie, S. G.; Hybertsen, M. S.; Neaton, J. B.; Venkataraman, L. *Nat. Nanotechnol.* **2009**, *4*, 230−234.
(25) van der Molen, S. J.; Liao, J.; Kudernac, T.; Agustsson, J. S.; Bernard, L.; Calame, M.; van Wees, B. J.; Feringa, B. L.; Schönenberger, C. *Nano Lett.* **2009**, *9*, 76−80.
(26) He, J.; Chen, F.; Liddell, P. A.; Andreasson, J.; Straight, S. D.; Gust, D.; Moore, T. A.; Moore, A. L.; Li, J.; Sankey, O. F.; Lindsay, S. M. *Nanotechnology* **2005**, *16*, 695−702.
(27) Jenny, N. M.; Mayor, M.; Eaton, T. R. *Eur. J. Org. Chem.* **2011**, 4965−4983.
(28) Baumgardt, I.; Butenschoen, H. *Eur. J. Org. Chem.* **2010**, 1076−1087.
(29) Kushmerick, J. G.; Holt, D. B.; Pollack, S. K.; Ratner, M. A.; Yang, J. C.; Schull, T. L.; Naciri, J.; Moore, M. H.; Shashidhar, R. *J. Am. Chem. Soc.* **2002**, *124*, 10654−10655.
(30) Chen, J.; Reed, M. A.; Rawlett, A. M.; Tour, J. M. *Science* **1999**, *286*, 1550−1552.
(31) Liao, J.; Bernard, L.; Langer, M.; Schönenberger, C.; Calame, M. *Adv. Mater. (Weinheim, Ger.)* **2006**, *18*, 2444−2447.
(32) Rawlett, A. M.; Hopson, T. J.; Nagahara, L. A.; Tsui, R. K.; Ramachandran, G. K.; Lindsay, S. M. *Appl. Phys. Lett.* **2002**, *81*, 3043−3045.
(33) Liu, K.; Li, G.; Wang, X.; Wang, F. *J. Phys. Chem. C* **2008**, *112*, 4342−4349.
(34) Beebe, J. M.; Kim, B.; Frisbie, C. D.; Kushmerick, J. G. *ACS Nano* **2008**, *2*, 827−832.
(35) Fan, F. R. F.; Yang, J. P.; Cai, L. T.; Price, D. W.; Dirk, S. M.; Kosynkin, D. V.; Yao, Y. X.; Rawlett, A. M.; Tour, J. M.; Bard, A. J. *J. Am. Chem. Soc.* **2002**, *124*, 5550−5560.
(36) Fracasso, D.; Valkenier, H.; Hummelen, J. C.; Solomon, G. C.; Chiechi, R. C. *J. Am. Chem. Soc.* **2011**, 9556−9563.
(37) Valkenier, H.; Huisman, E. H.; van Hal, P. A.; de Leeuw, D. M.; Chiechi, R. C.; Hummelen, J. C. *J. Am. Chem. Soc.* **2011**, *133*, 4930−4939.
(38) Cai, L. T.; Skulason, H.; Kushmerick, J. G.; Pollack, S. K.; Naciri, J.; Shashidhar, R.; Allara, D. L.; Mallouk, T. E.; Mayer, T. S. *J. Phys. Chem. B* **2004**, *108*, 2827−2832.
(39) Newton, M. D.; Smalley, J. F. *Phys. Chem. Chem. Phys.* **2007**, *9*, 555−572.
(40) Creager, S.; Yu, C. J.; Bamdad, C.; O'Connor, S.; MacLean, T.; Lam, E.; Chong, Y.; Olsen, G. T.; Luo, J. Y.; Gozin, M.; Kayyem, J. F. *J. Am. Chem. Soc.* **1999**, *121*, 1059−1064.
(41) Donhauser, Z. J.; Mantooth, B. A.; Kelly, K. F.; Bumm, L. A.; Monnell, J. D.; Stapleton, J. J.; Price, D. W.; Rawlett, A. M.; Allara, D. L.; Tour, J. M.; Weiss, P. S. *Science* **2001**, *292*, 2303−2307.
(42) Reichert, J.; Ochs, R.; Beckmann, D.; Weber, H. B.; Mayor, M.; von Lohneysen, H. *Phys. Rev. Lett.* **2002**, *88*, 176804.
(43) Mayor, M.; Weber, H. B.; Reichert, J.; Elbing, M.; von Hanisch, C.; Beckmann, D.; Fischer, M. *Angew. Chem., Int. Ed.* **2003**, *42*, 5834−5838.
(44) Huber, R.; González, M. T.; Wu, S.; Langer, M.; Grunder, S.; Horhoiu, V.; Mayor, M.; Bryce, M. R.; Wang, C. S.; Jitchati, R.; Schönenberger, C.; Calame, M. *J. Am. Chem. Soc.* **2008**, *130*, 1080−1084.
(45) Wu, S. M.; González, M. T.; Huber, R.; Grunder, S.; Mayor, M.; Schönenberger, C.; Calame, M. *Nat. Nanotechnol.* **2008**, *3*, 569−574.
(46) Xiao, X. Y.; Nagahara, L. A.; Rawlett, A. M.; Tao, N. J. *J. Am. Chem. Soc.* **2005**, *127*, 9235−9240.
(47) Liu, K.; Wang, X.; Wang, F. *ACS Nano* **2008**, *2*, 2315−2323.
(48) Hybertsen, M. S.; Venkataraman, L.; Klare, J. E.; Cwhalley, A.; Steigerwald, M. L.; Nuckolls, C. *J. Phys.: Cond. Matt.* **2008**, *20*, 374115.
(49) Weibel, N.; Mishchenko, A.; Wandlowski, T.; Neuburger, M.; Leroux, Y.; Mayor, M. *Eur. J. Org. Chem.* **2009**, 6140−6150.
(50) Xing, Y.; Park, T.-H.; Venkatramani, R.; Keinan, S.; Beratan, D. N.; Therien, M. J.; Borguet, E. *J. Am. Chem. Soc.* **2010**, *132*, 7946−7956.
(51) Lu, Q.; Liu, K.; Zhang, H. M.; Du, Z. B.; Wang, X. H.; Wang, F. S. *ACS Nano* **2009**, *3*, 3861−3868.
(52) Haiss, W.; Wang, C. S.; Grace, I.; Batsanov, A. S.; Schiffrin, D. J.; Higgins, S. J.; Bryce, M. R.; Lambert, C. J.; Nichols, R. J. *Nat. Mater.* **2006**, *5*, 995−1002.
(53) Martin, S.; Grace, I.; Bryce, M. R.; Wang, C.; Jitchati, R.; Batsanov, A. S.; Higgins, S. J.; Lambert, C. J.; Nichols, R. J. *J. Am. Chem. Soc.* **2010**, *132*, 9157−9164.
(54) González, M. T.; Leary, E.; Garcia, R.; Verma, P.; Angeles Herranz, M.; Rubio-Bollinger, G.; Martin, N.; Agrait, N. *J. Phys. Chem. C* **2011**, *115*, 17973−17978.
(55) Akkerman, H. B.; de Boer, B. *J. Phys.: Cond. Matt.* **2008**, *20*, 013001.
(56) Valkenier, H. Molecular Conductance: Synthesis, Assembly,and Electrical Characterization of π-Conjugated Wires and Switches. Ph.D. Thesis, Rijksuniversiteit, Groningen, July, 2011.
(57) Liu, H. M.; Wang, N.; Zhao, J. W.; Guo, Y.; Yin, X.; Boey, F. Y. C.; Zhang, H. *ChemPhysChem* **2008**, *9*, 1416−1424.
(58) Venkataraman, L.; Klare, J. E.; Nuckolls, C.; Hybertsen, M. S.; Steigerwald, M. L. *Nature* **2006**, *442*, 904−907.
(59) Wang, C. S.; Batsanov, A. S.; Bryce, M. R.; Martin, S.; Nichols, R. J.; Higgins, S. J.; García-Suárez, V. M.; Lambert, C. J. *J. Am. Chem. Soc.* **2009**, *131*, 15647−15654.
(60) Sedghi, G.; García-Suárez, V. M.; Esdaile, L. J.; Anderson, H. L.; Lambert, C. J.; Martin, S.; Bethell, D.; Higgins, S. J.; Elliott, M.; Bennett, N.; Macdonald, J. E.; Nichols, R. J. *Nat. Nanotechnol.* **2011**, *6*, 517−523.
(61) Yamada, R.; Kumazawa, H.; Noutoshi, T.; Tanaka, S.; Tada, H. *Nano Lett.* **2008**, *8*, 1237−1240.
(62) Quinn, J. R.; Foss, F. W. Jr.; Venkataraman, L.; Breslow, R. *J. Am. Chem. Soc.* **2007**, *129*, 12376−12377.
(63) Mishchenko, A.; Vonlanthen, D.; Meded, V.; Burkle, M.; Li, C.; Pobelov, I. V.; Bagrets, A.; Viljas, J. K.; Pauly, F.; Evers, F.; Mayor, M.; Wandlowski, T. *Nano Lett.* **2010**, *10*, 156−163.

(64) Mishchenko, A.; Zotti, L. A.; Vonlanthen, D.; Burkle, M.; Pauly, F.; Cuevas, J. C.; Mayor, M.; Wandlowski, T. *J. Am. Chem. Soc.* **2011**, *133*, 184−187.
(65) Stuhr-Hansen, N. *Synth. Commun.* **2003**, *33*, 641−646.
(66) Stuhr-Hansen, N.; Sørensen, J. K.; Moth-Poulsen, K.; Christensen, J. B.; Bjørnholm, T.; Nielsen, M. B. *Tetrahedron* **2005**, *61*, 12288−12295.
(67) Blaszczyk, A.; Elbing, M.; Mayor, M. *Org. Biomol. Chem.* **2004**, *2*, 2722−2724.
(68) van Dijk, E. H.; Myles, D. J. T.; van der Veen, M. H.; Hummelen, J. C. *Org. Lett.* **2006**, *8*, 2333−2336.
(69) Zhou, C. Z.; Liu, T. X.; Xu, J. M.; Chen, Z. K. *Macromolecules* **2003**, *36*, 1457−1464.
(70) Xu, B. Q.; Tao, N. J. J. *Science* **2003**, *301*, 1221−1223.
(71) Li, C.; Pobelov, I.; Wandlowski, T.; Bagrets, A.; Arnold, A.; Evers, F. *J. Am. Chem. Soc.* **2008**, *130*, 318−326.
(72) Muller, C. J.; Vanruitenbeek, J. M.; Dejongh, L. J. *Phys. Rev. Lett.* **1992**, *69*, 140−143.
(73) Hong, W.; Valkenier, H.; Meszaros, G.; Manrique, D. Z.; Mishchenko, A.; Putz, A.; Garcia, P. M.; Lambert, C. J.; Hummelen, J. C.; Wandlowski, T. *Beilstein J. Nanotechnol.* **2011**, *2*, 699−713.
(74) Meszaros, G.; Li, C.; Pobelov, I.; Wandlowski, T. *Nanotechnology* **2007**, *18*, 424004.
(75) Rocha, A. R.; García-Suárez, V. M.; Bailey, S.; Lambert, C.; Ferrer, J.; Sanvito, S. *Phys. Rev. B* **2006**, *73*, 085414.
(76) Rocha, A. R.; García-Suárez, V. M.; Bailey, S. W.; Lambert, C. J.; Ferrer, J.; Sanvito, S. *Nat. Mater.* **2005**, *4*, 335−339.
(77) Soler, J. M.; Artacho, E.; Gale, J. D.; Garcia, A.; Junquera, J.; Ordejon, P.; Sanchez-Portal, D. *J. Phys.: Cond. Matt.* **2002**, *14*, 2745−2779.
(78) Perdew, J. P.; Zunger, A. *Phys. Rev. B* **1981**, *23*, 5048−5079.
(79) Mowbray, D. J.; Jones, G.; Thygesen, K. S. *J. Chem. Phys.* **2008**, *128*, 111103.
(80) García-Suárez, V. M.; Lambert, C. J. *New J. Phys.* **2011**, *13*, 053026.
(81) Quek, S. Y.; Choi, H. J.; Louie, S. G.; Neaton, J. B. *Nano Lett.* **2009**, *9*, 3949−3953.
(82) González, M. T.; Wu, S.; Huber, R.; van der Molen, S. J.; Schönenberger, C.; Calame, M. *Nano Lett.* **2006**, *6*, 2238−2242.
(83) Agrait, N.; Yeyati, A. L.; van Ruitenbeek, J. M. *Phys. Rep.: Rev. Sec. Phys. Lett.* **2003**, *377*, 81−279.
(84) Martin, C. A.; Ding, D.; Sørensen, J. K.; Bjørnholm, T.; van Ruitenbeek, J. M.; van der Zant, H. S. J. *J. Am. Chem. Soc.* **2008**, *130*, 13198−13199.
(85) Weibel, N.; Blaszczyk, A.; von Haenisch, C.; Mayor, M.; Pobelov, I.; Wandlowski, T.; Chen, F.; Tao, N. *Eur. J. Org. Chem.* **2008**, 136−149.
(86) Xiao, X. Y.; Xu, B. Q.; Tao, N. J. *Nano Lett.* **2004**, *4*, 267−271.
(87) Martin, S.; Grace, I.; Bryce, M. R.; Wang, C. S.; Jitchati, R.; Batsanov, A. S.; Higgins, S. J.; Lambert, C. J.; Nichols, R. J. *J. Am. Chem. Soc.* **2010**, *132*, 9157−9164.
(88) Huang, Z.; Chen, F.; Bennett, P. A.; Tao, N. *J. Am. Chem. Soc.* **2007**, *129*, 13225−13231.
(89) Huang, Z.; Xu, B.; Chen, Y.; Di Ventra, M.; Tao, N. *Nano Lett.* **2006**, *6*, 1240−1244.
(90) Evans, E. *Annu. Rev. Biophys. Biomol. Struct.* **2001**, *30*, 105−128.
(91) Evans, E.; Ritchie, K. *Biophys. J.* **1997**, *72*, 1541−1555.
(92) Xu, B. Q.; Xiao, X. Y.; Tao, N. J. *J. Am. Chem. Soc.* **2003**, *125*, 16164−16165.
(93) Lafferentz, L.; Ample, F.; Yu, H.; Hecht, S.; Joachim, C.; Grill, L. *Science* **2009**, *323*, 1193−1197.
(94) Lörtscher, E.; Weber, H. B.; Riel, H. *Phys. Rev. Lett.* **2007**, *98*, 176807.
(95) Widawsky, J. R.; Kamenetska, M.; Klare, J.; Nuckolls, C.; Steigerwald, M. L.; Hybertsen, M. S.; Venkataraman, L. *Nanotechnology* **2009**, *20*, 434009.
(96) Malen, J. A.; Doak, P.; Baheti, K.; Tilley, T. D.; Segalman, R. A.; Majumdar, A. *Nano Lett.* **2009**, *9*, 1164−1169.
(97) Chen, F.; Li, X.; Hihath, J.; Huang, Z.; Tao, N. *J. Am. Chem. Soc.* **2006**, *128*, 15874−15881.
(98) Chen, F.; Li, X. L.; Hihath, J.; Huang, Z. F.; Tao, N. J. *J. Am. Chem. Soc.* **2006**, *128*, 15874−15881.
(99) Tomfohr, J.; Sankey, O. F. *J. Chem. Phys.* **2004**, *120*, 1542−1554.
(100) Wold, D. J.; Haag, R.; Rampi, M. A.; Frisbie, C. D. *J. Phys. Chem. B* **2002**, *106*, 2813−2816.
(101) Ishida, T.; Mizutani, W.; Aya, Y.; Ogiso, H.; Sasaki, S.; Tokumoto, H. *J. Phys. Chem. B* **2002**, *106*, 5886−5892.
(102) Beebe, J. M.; Kim, B.; Gadzuk, J. W.; Frisbie, C. D.; Kushmerick, J. G. *Phys. Rev. Lett.* **2006**, *97*, 026801.
(103) Veenstra, S. C.; Stalmach, U.; Krasnikov, V. V.; Hadziioannou, G.; Jonkman, H. T.; Heeres, A.; Sawatzky, G. A. *Appl. Phys. Lett.* **2000**, *76*, 2253−2255.
(104) Visontai, D.; Grace, I. M.; Lambert, C. J. *Phys. Rev. B* **2010**, *81*, 035409.
(105) Markussen, T.; Schioumltz, J.; Thygesen, K. S. *J. Chem. Phys.* **2010**, *132*, 224104.
(106) Markussen, T.; Stadler, R.; Thygesen, K. S. *Nano Lett.* **2010**, *10*, 4260−4265.
(107) Yanson, A. I.; Bollinger, G. R.; van den Brom, H. E.; Agrait, N.; van Ruitenbeek, J. M. *Nature* **1998**, *395*, 783−785.
(108) Toher, C.; Filippetti, A.; Sanvito, S.; Burke, K. *Phys. Rev. Lett.* **2005**, *95*, 146402.
(109) Ulrich, J.; Esrail, D.; Pontius, W.; Venkataraman, L.; Millar, D.; Doerrer, L. H. *J. Phys. Chem. B* **2006**, *110*, 2462−2466.
(110) Paulsson, M.; Krag, C.; Frederiksen, T.; Brandbyge, M. *Nano Lett.* **2009**, *9*, 117−121.
(111) Wang, C.; Bryce, M. R.; Gigon, J.; Ashwell, G. J.; Grace, I.; Lambert, C. J. *J. Org. Chem.* **2008**, *73*, 4810−4818.
(112) Papadopoulos, T. A.; Grace, I. M.; Lambert, C. J. *Phys. Rev. B* **2006**, *74*, 193306.
(113) Bratkovsky, A. M.; Kornilovitch, P. E. *Phys. Rev. B* **2003**, *67*, 115307.
(114) Dunbar, T. D.; Cygan, M. T.; Bumm, L. A.; McCarty, G. S.; Burgin, T. P.; Reinerth, W. A.; Jones, L.; Jackiw, J. J.; Tour, J. M.; Weiss, P. S.; Allara, D. L. *J. Phys. Chem. B* **2000**, *104*, 4880−4893.
(115) Liu, Z.; Wang, X.; Dai, K.; Jin, S.; Zeng, Z.-C.; Zhuang, M.-D.; Yang, Z.-L.; Wu, D.-Y.; Ren, B.; Tian, Z.-Q. *J. Raman Spectrosc.* **2009**, *40*, 1400−1406.